Instability of the one-dimensional thickness profile at the edge of a horizontal foam film and its Plateau border

Corentin Trégouët and Isabelle Cantat
Université Rennes, CNRS, IPR (Institut de Physique de Rennes)–UMR 6251, F-35000 Rennes, France

(Received 3 February 2021; accepted 13 October 2021; published 11 November 2021)

The thinning of the liquid films separating bubbles in a foam or in a bubbly liquid controls the coalescence process and the foam stability, and is highly relevant in many industrial processes. The spatiotemporal evolution of the film thickness is governed by highly nonlinear equations, the solution properties of which are still mostly unknown. For a flat film in contact with a meniscus at a lower pressure, a classical theoretical solution is the appearance, deepening and widening of a pinched region, uniform along the meniscus. However, film thinning has been shown to be mainly controlled by nonuniform marginal regeneration, for which no clear explanation has been provided to date. In this article, we establish experimentally that the theoretical uniform film thickness profile is unstable, even in a horizontal film, and we measure the instability wavelength along the meniscus. We show that the Poiseuille flow can be neglected during the destabilization process, and, taking advantage of this scale separation, we build an original equation set leading to the prediction of the instability wavelength.

DOI: 10.1103/PhysRevFluids.6.114005

I. INTRODUCTION

Liquid foams are complex fluids used in various industrial domains, such as food science, oil recovery, the cosmetic and detergent industry, ore extraction, or fire fighting. In most situations, the foam stability, i.e., its lifetime, is a key parameter; it is difficult to control or predict because the dynamics of film thinning is still poorly understood. The foam films consist of surfactant solution confined between two gas bubbles and limited laterally by a meniscus, as shown in Fig. 1(a). Their dynamics belongs to the large class of lubrication flows that are governed by a strong coupling between the shape of the limiting interfaces and the hydrodynamic forces. In the foam-film case, the coupling arises from the Laplace law [1], relating the interface curvature and the pressure: in the meniscus, the curvature is fixed by the bubble diameter and the total volume of the foaming solution, yielding a pressure lower than in the air; in the film, the thickness evolves with the flow of solution, generating a nonuniform curvature that gives a complex feedback on the flow. It results in a peculiar dynamics, and, depending on the boundary condition at the interfaces [2,3] and on the bubble motion, the meniscus under pressure may lead to different drainage processes: in particular, the thinnest part of the film may be either the film center [4–6] [Fig. 1(b)] or a pinched region at the film edge [7–10] [Fig. 1(c)]. In this last case, denoted *marginal pinching* in the literature, the film thickness profile has been predicted by Aradian, Raphaël, and de Gennes [2], assuming the interfaces do not move. This important simplification actually results from two different assumptions: (i) an incompressible interface, which is a limit usually reached in foam films, due to their high interface elastic modulus [11], and (ii) the uniformity of the profile along the meniscus direction, which only results from the symmetry of the problem. These two conditions impose a uniform velocity at the interface, and thus a velocity equal to zero on the whole interface when the film is at rest far from the meniscus. The aim of the paper is to question the

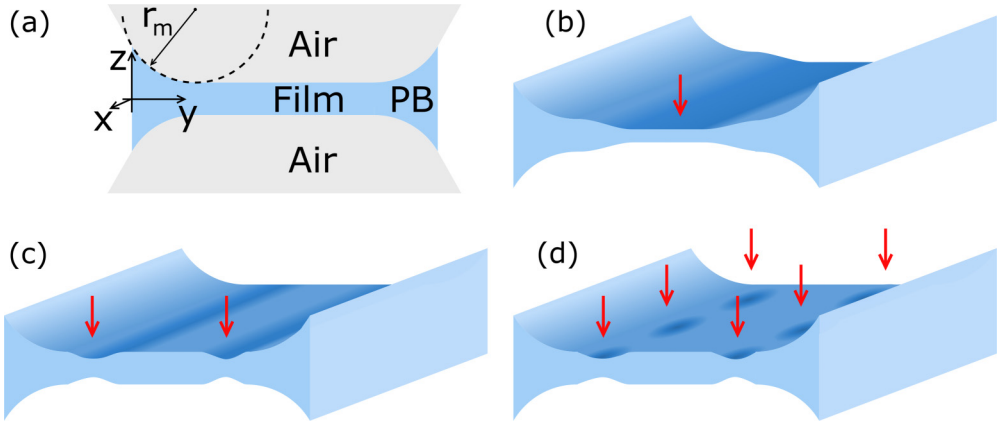

FIG. 1. (a) Sketch of the studied configuration: a flat film of surfactant solution separates two volumes of air (bubbles), and is delimited by two Plateau borders (PBs) of uniform radius of curvature r_m. Under the assumption of a thickness uniform along the x direction, different cases are known for the drainage depending on the boundary condition at the interfaces: the thinnest part of the film can be located in the center (b) or at the edges of the film (c). In the experiments and in the present modeling, the thickness profile is close to case (c) at short time. However, it does not remain uniform along the x direction at long time, and it destabilizes into a periodic pattern (d).

assumption (ii) and to investigate the stability of the one-dimensional (1D) profile with respect to 2D perturbations.

We first recall here the mechanism detailed in [2] leading to the pinched regions close to the meniscus [see Fig. 1(c)]. A meniscus (also called a *Plateau border*) of uniform radius of curvature r_m is oriented along x and in contact with a flat immobile film of thickness $2h_\infty$ at large y. The film is horizontal, so there are no gravity effects, and it is thick enough for the disjoining pressure to be negligible. The pressure in the film at the position y is thus entirely controlled by the Laplace pressure, which is the product of the interfacial tension γ and of the interface curvature. The Reynolds number is negligible, and the pressure gradient balances the viscous forces associated with the Poiseuille flow in the film. Due to volume conservation, the flow, which is driven by the thickness profile, also modifies the thickness. This complex feedback loop generates the following dynamics: at the edge between the flat film at atmospheric pressure and the meniscus at a lower pressure, there is a flow from the film to the meniscus. This flow decreases the thickness at the film edge and creates a trough and a new pressure distribution along the film, with a low pressure at the bottom of the trough and a high pressure at its border. The subsequent fluxes result in a widening and a deepening of the trough. The modeling discussed in Sec. IV yields at long time to a scale invariant film profile, with scaling laws for the characteristic width w of the pinched region and for the minimal thickness $h_{\min}$ of the profile as a function of time t:

$$w \sim r_m \left(\frac{t}{\tau}\right)^{1/4} \tag{1}$$

and

$$h_{\min} \sim \frac{h_\infty^2}{r_m}\left(\frac{t}{\tau}\right)^{-1/2}, \tag{2}$$

with τ being a viscocapillary time such as $\tau = 3\eta r_m^4/(\gamma h_\infty^3)$, where η is the viscosity of the liquid. In this mechanism, the flow is 1D, and the thickness profile remains uniform in the direction parallel to the meniscus.

This process is at the origin of the dimple shapes often observed in draining films [12]. In some cases, the pinched region is reported to destabilize into a necklace of thin spots [13–15], and this instability then evolves into a nonuniform flow dynamics along the meniscus [1,16,17], which controls the subsequent film drainage and its lifetime [10,18–20]: regions of the film with a small thickness are emitted from the menisci, while thicker parts of the film flow into the menisci. In the presence of gravity, the thin regions migrate by buoyancy to the top of the film. The localization of this phenomenon at the margin of the film yielded the term *marginal regeneration* [1]. The identification of the parameters controlling the destabilization process, and the prediction of the initial wavelength, are open questions in the literature.

Symmetry breaking induced by the disjoining pressure [21] or by an increase of the tension far from the meniscus, due to evaporation in a binary mixture [22], has been observed. In this paper, we show that the film profile destabilization occurs even in the absence of gravity or disjoining pressure, and that it can be explained by capillary effects only. We produce a 600-nm-thick horizontal film at rest, in contact with a meniscus. A thinner region appears along the meniscus, initially uniform by translation along the meniscus, and this pinched region destabilizes into quasicircular spots of thin film separated by a well-defined wavelength. Revisiting the classical lubrication equations, we show that this destabilization occurs by a simple reorganization of the film elements in the plane of the film, driven by the interface area minimization, under the novel constraint that the film thickness distribution must be preserved. Under well-controlled approximations, we show that the instability is entirely decoupled from the underlying drainage process, which allows us to predict the scaling laws for the instability wavelength, in qualitative agreement with our observations. The wavelength later increases due to a coarsening process studied in [17].

II. EXPERIMENTAL SETUP

A. Physicochemical properties of the foaming solution

The foaming solution consists of water, with 15 %w glycerol, 5.6 g/L of sodium dodecyl sulfate (cmc: 2.36 g/L), and 0.8 g/L fluorescein. The resulting viscosity is 1.5 mPa s and the surface tension is $\gamma = 40$ mN/m. The surface shear viscosity is not known with a high degree of precision, and the values reported in the literature show a large dispersion [23]. Here we assume $\eta_s = 6 \times 10^{-8}$ kg s, following [24]. The hygrometry is not controlled, and the evaporation may lead to a slow increase of the initial concentrations. A thickness decrease rate of 30 nm/s may be deduced from [25] for horizontal interfaces of a surfactant solution of comparable area, and for a relative humidity of 50%. This should not play any role during the destabilization time.

B. Mechanical and optical devices

Our experimental setup is similar to the setup used in [17], in which the experimental details are given. A deformable frame holds three rectangular, flat, foam films connected by a free meniscus (or *Plateau border*). The film of interest is horizontal, of constant dimension L_x in the x direction and variable dimension L_y in the y direction (see Fig. 2). Its dynamics is monitored through two cameras. A Photron S4 fast camera, perpendicular to the film, records the fluorescent signal thanks to a blue LED illumination and a dichroic filter (1000 fps, 5 μm/pixel). The film thickness, as well as the meniscus width, are measured from these images. A Resonon Pika L spectral camera provides a better determination of the height profile along a line perpendicular to the free meniscus by specular reflection of a halogen light forming an angle of 48° with the vertical direction (100 fps, 2.5 μm/pixel).

C. Film preparation

The three motor displacements are tuned to produce a horizontal film close to the ideal initial conditions discussed in Ref. [2]: a film of uniform thickness and vanishing interface velocity, in

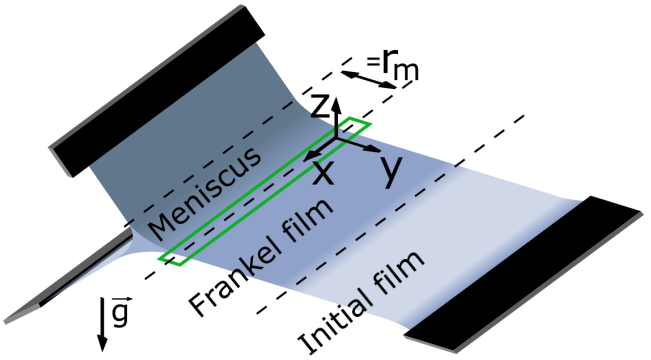

FIG. 2. Sketch of the experimental setup. Three films extend between a free meniscus and mobile frames, and the film of interest is the horizontal one in the xy plane. To produce a reproducible initial condition, a piece of film of controlled thickness (of the order of one micron), denoted as the *Frankel film*, is extracted from the free meniscus by stretching the horizontal film. The green rectangle represents the area of interest pictured in Fig. 4. The meniscus on the mobile frame (on the right) behaves similarly but is not studied.

contact with a static meniscus. Toward this end, the frame is plunged into the solution, producing the three *initial films*. Then the horizontal film is stretched and the lateral films are compressed by moving the motors at a speed of 50 mm/s. The tension increases in the horizontal film, and some new film is extracted from the meniscus, following Frankel's law [1]. The thickness of the new film, located between the initial film and the meniscus, and denoted as *Frankel's film* in the following, is of the order of 600 nm, so that the disjoining pressure is negligible. If the motor is suddenly stopped, the film extraction continues as long as the horizontal film tension is above its steady value. The extraction velocity, and thus Frankel's film thickness, decreases during the tension relaxation process, and the flat film's initial condition is therefore not achieved. A much better result is obtained by moving the motors back by a small amount after the stretching step. This relaxes the film tension and stops the film extraction more rapidly. The boundary between the initial film and Frankel's film (c-d limit in Fig. 3) starts receding at the time $t = t_i$ defined as the initial time of the experiment. As discussed below, the interface velocity vanishes close to the meniscus at an intermediate time, after the motor stop and before t_i. The instability of interest occurs typically 0.5 s later than t_i.

Following two characteristic material points in the film (the point of maximal thickness and the boundary between Frankel's film and the initial film), we estimate the compression rate during this relaxation as $\dot{\varepsilon} = 2 \pm 1\ \mathrm{s}^{-1}$, which is consistent with the compression rate deduced from the thickness map in Sec. IV B. Assuming a homogeneous compression in the film, the velocity, extrapolated at the boundary with the meniscus, is lower (in absolute value) than 0.5 mm/s. The upper bound for the interface displacement in the pinched region during the 20 ms of the destabilization process is therefore 10 μm, i.e., a small fraction of the width of the profile. The best evidence of the vanishing velocity at the meniscus results from the analysis in Sec. IV B. In the following, we thus assume that the interface velocity is vanishing at the meniscus during the destabilization.

The region of interest is located in Frankel's film, close to the free meniscus. In this domain, the film thickness is uniform at t_i, with a value of $2h_\infty$. This thickness has been varied in the range [0.5, 1] μm and is correlated with the meniscus radius r_m, which is in the range [375, 570] μm. From this initial condition, we let the film evolve spontaneously.

D. Initial film profile characterization

The film first remains uniform in the x direction and gets locally thinner at the boundary between the meniscus and the film. Then, at a critical time, chosen as the reference time $t = 0$ (note that this

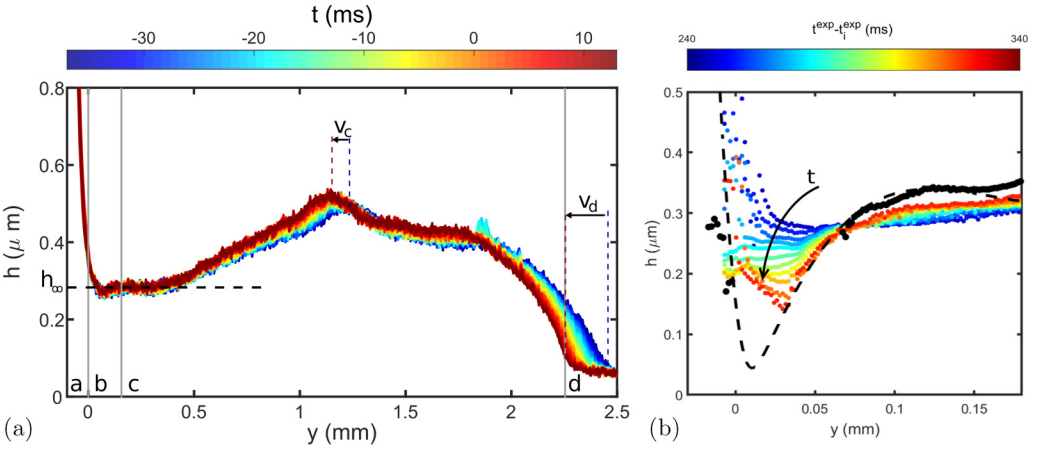

FIG. 3. (a) Film profile (h is the half-thickness) from fluorescence measurement calibrated through the spectral camera, close to the destabilization time at $t = 0$ (in this example, $t_i = -450$ ms). Areas a, b, c, and d, respectively, correspond to the meniscus, the pinched region, the Frankel film, and the initial thin film. Two characteristic material points can be followed during this time range and move at the velocities $v_c = 1.6$ mm/s and $v_d = 4.0$ mm/s indicated in the figure, showing the film compression. (b) Zoom on the 1D film profiles obtained with the spectral camera for the same experiment, before the destabilization. The colored profiles are recorded from $t = -210$ ms (dark blue) to -110 ms (red) every 10 ms, and the black one show the measurable part of the profile at $t = 0$ ms.

implies $t_i < 0$), the uniformity in the x direction is spontaneously broken, and the pinched region begins to destabilize in small circular patches of thin film surrounded by the film of thickness $2h_\infty$ (see Fig. 4). The film half-thickness profiles $h^{\exp}(y, t)$ obtained with the spectral camera at different times between $t = t_i$ and the time $t = 0$ are shown in Fig. 3. The profiles at short time are entirely resolved, but when thickness gradients become too large, or the thickness too thin, the interference pattern is lost. In particular, at the destabilization time the thinnest part of the profile is not measured. Few data points are obtained on the meniscus side, and they show a fast increase of the thickness, as expected. This enables us to localize precisely the meniscus. On the film side, the upper part of the profile is resolved.

E. Instability wavelength and destabilization time

We now focus on the destabilization of the film profile at $t > 0$. The fluorescence intensity along a line $y = y_p$ close to the meniscus (see Fig. 4) is plotted for different times in Fig. 5. We define $\lambda_{\exp}$ as the wavelength measured on the first profile where an oscillating intensity can be detected.

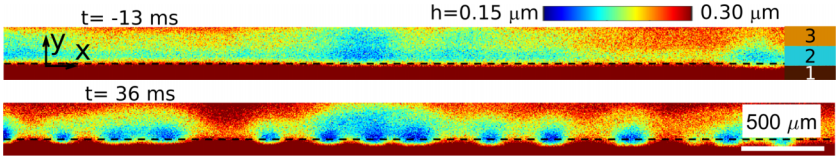

FIG. 4. Film thickness field obtained from the fluorescence intensity before (top, $t = -13$ ms) and after (bottom, $t = 36$ ms) the instability onset (h is the half-thickness). The bars on the right of the top image indicate the meniscus (region 1, thickness not resolved), the pinched region, of width w_p (region 2), and Frankel's film, of thickness $2\,h_\infty$ (region 3). The region pictured corresponds to the rectangle shown in Fig. 2, and the dashed line is the position y_p where the profiles of Fig. 5 are measured.

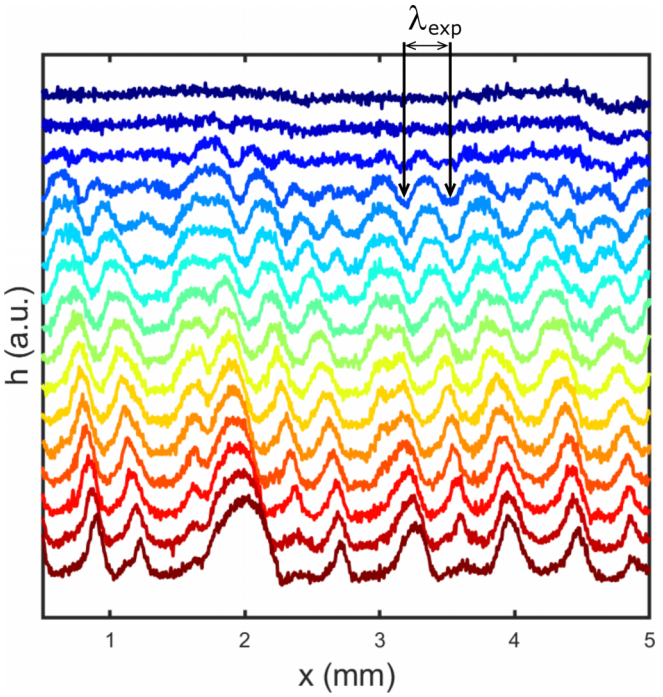

FIG. 5. Intensity profiles along the line $y = y_p$ (shown in Fig. 4) recorded every 10 ms, from $t = 0$ (top, dark blue) to $t = 150$ ms (bottom, dark red). An arbitrary offset is added for the sake of visibility.

More precisely, in profiles like the one presented in Fig. 5, we identify patterns consisting of a few wavelengths that grow simultaneously over time, and we measure the wavelength at the first instant that it can be detected. The resulting measurements are presented as a function of the half-thickness of the flat film, h_∞, in Fig. 6.

III. THEORY

We consider a film of half-thickness $h(x, y)$ as schematized in Fig. 7. As in the model of Mysels *et al.* [1], we assume the Gibbs elasticity to be large enough so that the limit of incompressible interface is reached [11,26]. The interface is therefore seen as a two-dimensional incompressible Newtonian fluid, of interface shear viscosity η_s and of tension $\gamma = \gamma_0 + \delta\gamma(x, y, t)$, with γ_0 a reference tension, taken as the equilibrium tension of the foaming solution. In this limit, the tension variation $\delta\gamma$ is not related to any thermodynamic property of the interface, and it can be seen as the Lagrange multiplier associated with the conservation of the local interface area. This model has been introduced by Mysels *et al.* [1] to describe the motion of the interfaces defined as "mobile." This must not be confused with the "rigid" interfaces, which follow similar rules but with an infinite shear viscosity that prevents any recirculation in the film.

A. Lubrication equations

The lubrication equations governing the bulk velocity $\mathbf{u}(x, y, z, t)$ and the half film thickness $h(x, y, t)$ have been established in [16,27] and are briefly recalled here. They can be derived from the 3D Stokes equation by making a Taylor expansion, using $\varepsilon = h/L$ as a small parameter, with L the characteristic length scale of the thickness variations. At dominant order, the normal velocity

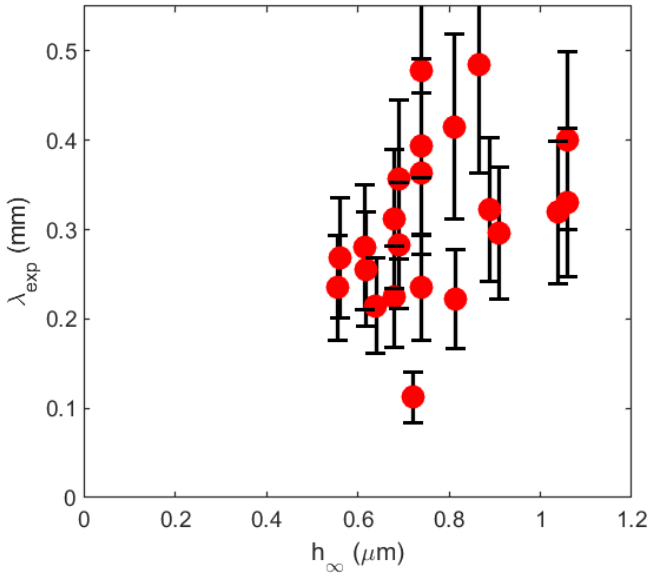

FIG. 6. Measured wavelengths as a function of the half-thickness of the flat Frankel film.

is negligible and $\mathbf{u} = (u_x, u_y)$; the pressure is uniform across the film, and its value is $P(x, y) = -\gamma_0 \Delta h$, with Δh the interface mean curvature (note that Δ and $\boldsymbol{\nabla}$ are 2D operators).

The Stokes equation $\eta\, \partial^2 \mathbf{u}/\partial z^2 = \boldsymbol{\nabla} P$ leads to, by successive integrations,

$$\frac{\partial \mathbf{u}}{\partial z} = -\frac{\gamma_0}{\eta} \boldsymbol{\nabla}(\Delta h)\, z, \tag{3}$$

$$\mathbf{u} = -\frac{\gamma_0}{\eta} \boldsymbol{\nabla}(\Delta h) \left(\frac{z^2}{2} - \frac{h^2}{2} \right) + \mathbf{v}, \tag{4}$$

$$\mathbf{q} = \int_0^h \mathbf{u}\, dz = \frac{\gamma_0}{3\eta} h^3 \boldsymbol{\nabla}(\Delta h) + \mathbf{v}h. \tag{5}$$

Equation (3) is obtained using the symmetry condition in the middle of the film, $\partial \mathbf{u}/\partial z(0) = 0$, and Eq. (4) uses the boundary condition $\mathbf{u}(h) = \mathbf{u}(-h) = \mathbf{v}$.

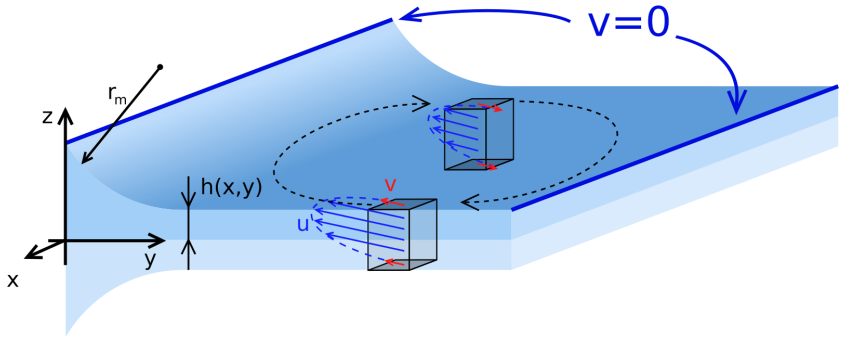

FIG. 7. Notations used in the text and schematic of the most general flow pattern, associated with Eqs. (3)–(5).

The mass conservation in the film gives finally

$$\frac{\partial h}{\partial t} = -\nabla \cdot \left[\frac{\gamma_0}{3\eta} h^3 \nabla(\Delta h) + \mathbf{v} h \right]. \tag{6}$$

The interface velocity $\mathbf{v}(x, y, t)$ is determined from the condition of tangential stress continuity at the interface [16]:

$$\gamma_0 h \nabla(\Delta h) + \eta_s \Delta \mathbf{v} + \nabla \delta\gamma = 0. \tag{7}$$

This equation can be seen as the Stokes equation for the interface, modeled as a 2D Newtonian incompressible fluid. The term $\eta_s \Delta \mathbf{v}$ represents the viscous forces in the interface, in the limit of small interface curvature, and the term $\nabla \delta\gamma$ is the 2D equivalent of a pressure term, insuring the interface incompressibility. The first term has no 3D equivalent, as it arises from the friction between the interface and the underlying fluid, which is proportional to the bulk velocity derivative given by Eq. (3).

For an interface element of projected area $dS = dx\,dy$, the actual area is

$$dA = \sqrt{1 + (\nabla h)^2}\, dx\, dy \sim dx\, dy + \tfrac{1}{2}(\nabla h)^2 dx\, dy. \tag{8}$$

At dominant order, the conservation of dA implies that $dx\,dy$ must be conserved, leading to the condition $\nabla \cdot \mathbf{v} = \mathbf{0}$. This condition can be taken into account by using the stream function $\psi(x, y)$ defined such as $\mathbf{v} = (\frac{\partial \psi}{\partial y}, -\frac{\partial \psi}{\partial x})$. After derivation of both components of Eq. (7), they are combined into

$$\eta_s \left(\frac{\partial^4 \psi}{\partial x^4} + 2 \frac{\partial^4 \psi}{\partial x^2 y^2} + \frac{\partial^4 \psi}{\partial y^4} \right) = \gamma_0 \left(\frac{\partial h}{\partial x} \frac{\partial \Delta h}{\partial y} - \frac{\partial h}{\partial y} \frac{\partial \Delta h}{\partial x} \right). \tag{9}$$

The film dynamics is thus governed by the coupled Eqs. (6) and (9), once initial and boundary conditions have been set.

B. Solutions with vanishing interface velocities

Let us first remark that Eq. (9) imposes that solutions with vanishing interface velocity verify

$$\frac{\partial h}{\partial x} \frac{\partial \Delta h}{\partial y} - \frac{\partial h}{\partial y} \frac{\partial \Delta h}{\partial x} = 0. \tag{10}$$

It follows immediately that any profile uniform along x belongs to this class of solutions, and is thus compatible with the condition $\mathbf{v} = \mathbf{0}$.

In this 1D case, the equations set (6),(9) simplifies into Eq. (6) only, in its 1D version and with $\mathbf{v} = 0$. As discussed in the Introduction, this case has been solved by Aradian *et al.* [2] to predict the evolution of a foam film in contact with a straight meniscus, assuming *a priori* a solution uniform along the meniscus. This situation corresponds to our experimental case, before the instability onset, and the corresponding equation is solved numerically in Sec. IV A to analyze our initial condition.

The condition $\mathbf{v} = \mathbf{0}$ is also compatible with axisymmetric shapes. Indeed, Eq. (10) can be written in polar coordinates (r, θ) as

$$\begin{aligned} &\left(\sin\theta \frac{\partial h}{\partial r} + \frac{1}{r \sin\theta} \frac{\partial h}{\partial \theta} \right) \left(\cos\theta \frac{\partial \Delta h}{\partial r} - \frac{1}{r \sin\theta} \frac{\partial \Delta h}{\partial \theta} \right) \\ &\quad = \left(\cos\theta \frac{\partial h}{\partial r} - \frac{1}{r \sin\theta} \frac{\partial h}{\partial \theta} \right) \left(\sin\theta \frac{\partial \Delta h}{\partial r} + \frac{1}{r \sin\theta} \frac{\partial \Delta h}{\partial \theta} \right), \end{aligned} \tag{11}$$

which is verified for any function $h(r)$ invariant with θ.

If such symmetries are *a priori* assumed in a foam film, the condition $\mathbf{v} = \mathbf{0}$ at the interface is automatically verified: the condition of a "rigid interface," valid at large interface shear viscosity, is artificially recovered, without any assumption on the interface shear viscosity value. In contrast,

for a generic profile $h(x, y)$, the hydrodynamic problem does not have any solution at vanishing interface velocity, and Eq. (9), involving η_s, must be solved.

C. The sliding puzzle dynamics

At this stage, we propose the key approximation of the paper, based on a scale separation between the Poiseuille flux, damped by the bulk viscosity, and the flux due to the in-plane recirculation, damped by the interface viscosity.

Assuming that the thickness and velocity variations occur on the characteristic length scale L in both directions x and y, the comparison of the two terms of Eq. (9) imposes the scaling of the interfacial velocity $v \sim (\gamma_0 h/\eta_s)h/L$. We can then substitute this scaling in Eq. (6) and compare the fluxes associated with the Poiseuille flow and with the recirculation at velocity v. The first one is much smaller than the second one if $L \gg L^{\mathrm{spd}}$, with

$$L^{\mathrm{spd}} = h\sqrt{\frac{\eta_s}{h\,\eta}} \tag{12}$$

a critical length, of the order of 10 μm if $h \sim 1$ μm and $\eta_s = 6 \times 10^{-8}$ kg s^{-1}. The small value of L^{spd} makes such dynamics, hereafter denoted as the *sliding-puzzle dynamics*, relevant for a large class of dynamical problems in foam films. It leads to original and simplified equations of motion, which may allow us to solve problems that are otherwise difficult to address.

In such a regime, Eq. (6) becomes

$$\frac{\partial h}{\partial t} = -\boldsymbol{\nabla}\cdot(\mathbf{v}h) = -\mathbf{v}\cdot\boldsymbol{\nabla}h. \tag{13}$$

The bulk velocity is homogeneous across the film, equal to $\mathbf{v}$, so an elementary volume $d\Omega = 2h\,dS$, denoted a *film element* in the following, is a closed material system of constant volume. The projected area dS is conserved (at leading order in h/L), and thus h is conserved too and behaves as a passive tracer. The position of a given element in the film, and its shape, may nevertheless vary, one element replacing the other in the film plane, as in a sliding puzzle.

We define the film half-thickness distribution as

$$\hat{S}(h_0) = \int_S H(h_0 - h(x, y))dx\,dy, \tag{14}$$

with H the Heaviside function, and $\hat{S}(h_0)$ is the projected area of the domain having a half-thickness smaller than h_0, in the domain S of interest. During a sliding-puzzle dynamics, this distribution is conserved, as h is conserved for each element. However, the motion modifies the thickness gradients and induces interface area variations of the order of $(\boldsymbol{\nabla}h)^2$. In the following, we show that these higher-order area variations generate the driving forces for spontaneous in-plane reorganizations of the film.

D. Energy balance

When the Poiseuille flow is negligible, the dissipation in the bulk can be neglected in the energy balance of a domain Ω of the film. Moreover, if we assume a vanishing interface velocity at the boundary of the system, the tension forces related to $\delta\gamma$ do not provide power to the system. The energy balance, to be derived just below, is thus simply

$$\gamma_0\frac{dA}{dt} + D_s = 0, \tag{15}$$

with D_s the viscous dissipation induced in an interface by the flow.

Despite the apparent simplicity of this equation, rigorously writing the energy balance in capillary flows is not straightforward, as discussed in [28], even for a clean interface with vanishing elasticity. Equation (15) can be established from a scalar product between Eq. (7) and the velocity

field $\mathbf{v}$, integrated spatially. Using the assumption that $\mathbf{v}$ is vanishing at the integration domain boundary and that Eq. (13) applies, the three terms in Eq. (7) are computed using several times the relation $\int \mathbf{A} \cdot \nabla B = -\int B \, \mathrm{div}\mathbf{A}$, valid when $\mathbf{A}$ or B is vanishing at the boundary,

$$\begin{aligned} I_1 &= \int_S \gamma_0 \, h \nabla(\Delta h) \cdot \mathbf{v} \, dx \, dy \\ &= -\gamma_0 \int_S \Delta h \, \mathbf{v} \cdot \nabla h \, dx \, dy \\ &= \gamma_0 \int \nabla h \cdot \nabla(\mathbf{v} \cdot \nabla h) \, dx \, dy \\ &= -\gamma_0 \int \nabla h \cdot \nabla \left(\frac{dh}{dt} \right) dx \, dy \\ &= -\gamma_0 \frac{dA}{dt}, \end{aligned} \tag{16}$$

$$\begin{aligned} I_2 &= \int_S \eta_s \Delta \mathbf{v} \cdot \mathbf{v} \, dx \, dy \\ &= -\eta_s \int_S \left((\nabla v_x)^2 + (\nabla v_y)^2 \right) dx \, dy \\ &= -D_s, \end{aligned} \tag{17}$$

and finally

$$I_3 = \int_S \nabla \delta\gamma \cdot \mathbf{v} \, dxdy = 0, \tag{18}$$

which leads to Eq. (15).

In the limit $L \gg L^{\mathrm{spd}}$, and at the order 2 in h/L, the film in-plane reorganizations are entirely decoupled from the bulk properties. They are driven by the area minimization and damped by the interface viscosity; they are, however, governed by the Marangoni Eq. (7), which involves the friction on the bulk (first term) and the tension gradient (third term).

E. The symmetric increasing rearrangement and the Pólya-Szegö inequality

We deduce from Eq. (15) that the stable shapes are minimal surfaces under the constraint of conserved area distribution. The Pólya-Szegö inequality (Ref. [29], Chap. 3) discussed below implies that the most stable profile in this situation is the axisymmetric one.

This inequality applies to an initial film profile $h(x, y) = h_\infty - \delta h(x, y)$ (with $\delta h > 0$ defined in the whole plane) under the assumption that $(\delta h)^2$ is integrable, as well as the square of its gradient. Note that this excludes the x-invariant film profiles.

Let us define the *Schwarz symmetric increasing rearrangement* $h^s(r)$ of the initial film profile $h(x, y)$ as the unique axisymmetric shape that has the same half-thickness distribution $\hat{S}$ and that increases with the distance r to the origin. The profile h^s is simply obtained by a rearrangement of the initial film elements of h, from the thinnest at small r to the thickest at larger r, in concentric domains. It is an axisymmetric pinched region in the middle of a flat film of asymptotic thickness h_∞.

The Pòlya-Szegö inequality states that

$$\int (\nabla h)^2 \, dx \, dy \geqslant \int (\nabla h^s)^2 \, dx \, dy. \tag{19}$$

Using the expression of the film area Eq. (8), this inequality proves that among all the shapes accessible by a sliding puzzle dynamics from the initial shape h, the symmetric increasing

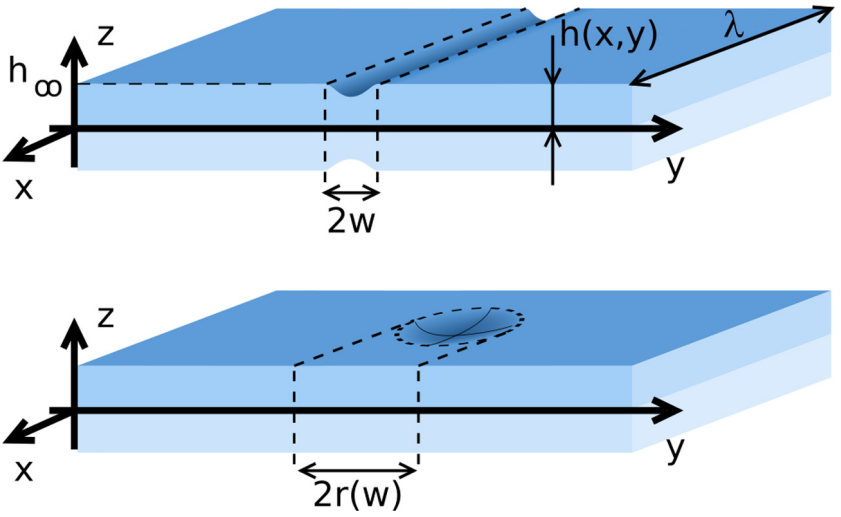

FIG. 8. The Gaussian profile in the domain $\mathcal{P}_\lambda$ (top) and its reorganized axisymmetric shape (bottom).

rearrangement h^s of h has the smallest area and is thus the most stable shape. This theorem ensures the global stability of a single axisymmetric increasing film profile $h(r)$ for the dynamics of interest. It can be extended to the metastability of a set of such axisymmetric profiles, as long as the pinched regions are separated from each other by a flat film of reference thickness h_∞.

The case of an x-invariant film profile cannot be directly discussed using the same tool, as it does not belong to the allowed class of profiles. However, a direct comparison between the energy of an x-invariant pinched region and the energy of a set of isolated axisymmetric pinched regions can be done: if the energy of the latter profile is lower, the spontaneous destabilization of the x-invariant profile toward this metastable solution is possible, otherwise it is not.

F. Example of Gaussian profiles and scaling law

In this section, we consider the simple case of an infinite flat foam film, with a thinner part in the vicinity of the x axis. We assume the thickness profile to be uniform in the x direction and Gaussian in the y direction. This differs from our experimental geometry, but it provides an illustrative and analytically solvable example. The aim is to compare the interfacial energy of this shape with the energy of shapes, nonuniform in the x direction, and in which the thinner part of the first film has been rearranged into a necklace of locally axisymmetric thin patches, with conservation of the thickness distribution. We show that, depending on the wavelength, these nonuniform shapes may be more or less stable than the first one.

Consider an x-invariant Gaussian pinched region of width w and depth h_0,

$$h_{\rm lin}(x,y) = h_\infty - h_0 e^{-y^2/(2w^2)}, \tag{20}$$

and a band of film $\mathcal{P}_\lambda$ of length λ in the x direction and spanning from $y=-\infty$ to $+\infty$ (see Fig. 8).

The excess area of the piece of film located in $\mathcal{P}_\lambda$, with respect to a flat film in the same domain, is, at dominant order,

$$\delta A_{\rm lin} = \lambda \int_{-\infty}^{\infty} \frac{1}{2}\left(\frac{\partial h}{\partial y}\right)^2 dy = \lambda \frac{h_0^2\sqrt{\pi}}{4w}. \tag{21}$$

An axisymmetric profile $h_{{\rm axi},\lambda}$ is then produced by a spatial reorganization of the film elements located in $\mathcal{P}_\lambda$. For a given y, all the film elements with a thickness smaller than $h_{\rm lin}(y)$ are in a rectangular domain of width $2y$ and length λ, and hence of projected area $2\lambda y$. After rearrangement,

this rectangle becomes a circular domain of the same area, and hence of radius $r(y)$ such as $\pi r(y)^2 = 2\lambda y$.

Before and after rearrangement, the maximum thicknesses are at the edge of the domains, and therefore

$$h_{\mathrm{axi},\lambda}(r(y)) = h_{\mathrm{lin}}(y) = h_{\mathrm{lin}}(\pi r(y)^2/(2\lambda)) \tag{22}$$

$$h_{\mathrm{axi},\lambda}(r) = h_\infty - h_0 e^{-\pi^2 r^4/(8\lambda^2 w^2)}. \tag{23}$$

The excess area of this shape is

$$\delta A_{\mathrm{axi},\lambda} = \pi \int_0^\infty \left(\frac{\partial h_{\mathrm{axi},\lambda}}{\partial r}\right)^2 r\, dr = \pi h_0^2, \tag{24}$$

and is thus more favorable than the initial 1D profile if

$$\lambda > \lambda_G^* = 4\sqrt{\pi} w. \tag{25}$$

The same transformation is made for every band of width λ, leading to a set of axisymmetric pinched regions. They are not strictly isolated, but the obtained pinched regions can be distributed in the (x, y) plane to ensure that they are separated by a film of thickness as close as we want to h_∞.

For example, if the axisymmetric shape obtained for λ_G^* has its center of symmetry in the middle of $\mathcal{P}$, its value at the boundary of $\mathcal{P}$ is

$$h_\infty - h_{\mathrm{axi}}(r = \lambda_G^*/2) = h_0\, e^{-\pi^2(\lambda_G^*)^2/(2^7 w^2)} \tag{26}$$

$$= h_0\, e^{-\pi^3/8} = 0.02 h_0. \tag{27}$$

As the asymptotic thickness is almost recovered, this axisymmetric shape can be restricted to the domain $\mathcal{P}_\lambda$ without significant modification of $\hat{S}$. It can then be used as an elementary pattern to built a periodic film profile of wavelength λ, with the axisymmetric pinched regions distributed along a straight line. This remark is valid for any $\lambda > \lambda_G^*$.

Finally, a Gaussian profile, uniform in the x direction and of width w, can destabilize into a row of axisymmetric spots if the associated wavelength is larger than $\lambda_G^* = 4\sqrt{\pi} w$. These rows of axisymmetric Gaussian spots are metastable shapes whose total energy (per unit length in the x direction) decreases with the wavelength. This criterion is of a purely geometric nature, and the smallest allowed wavelength is proportional to the pinched region width, with a simple numerical prefactor. Note that the dynamics has been entirely disregarded in this analysis, so this stability criterion only provides a necessary condition for the destabilization, and λ_G^* is a lower bound for the observed wavelength.

This result can be extended to an arbitrary profile, characterized by a depth h_p and a width w_p, using scaling analysis. Indeed, the excess area of a length λ of the pinched region is $\delta A_{\mathrm{lin}} \sim \lambda w_p (h_p/w_p)^2 = \lambda h_p^2/w_p$, whereas for the corresponding axisymmetric shape, the gradients are built on the radius of the disk, $r_p = \sqrt{\lambda w_p}$, so $\delta A_{\mathrm{axi},\lambda} \sim \lambda w_p (h_p/r_p)^2 = h_p^2$. The two excess areas are thus equal if $\lambda \sim w_p$, which provides the scaling of the instability wavelength.

IV. COMPARISON WITH EXPERIMENTAL DATA

The experimental observations can now be rationalized, on the basis of the theoretical arguments developed in Sec. III. When the interfacial velocity vanishes, the film begins to get thinner along the meniscus. This slow dynamics results from a Poiseuille flow, without velocity at the interface, and is governed by Eq. (6) in its 1D version. It leads to the x-invariant film profile that eventually destabilizes at $t = 0$. This first step is discussed in Sec. IV A. We then address the destabilization process, which involves nonzero interfacial velocities, 2D recirculation at large scale, and a negligible contribution of the Poiseuille flow. This second step obeys the simplified Eq. (15), based

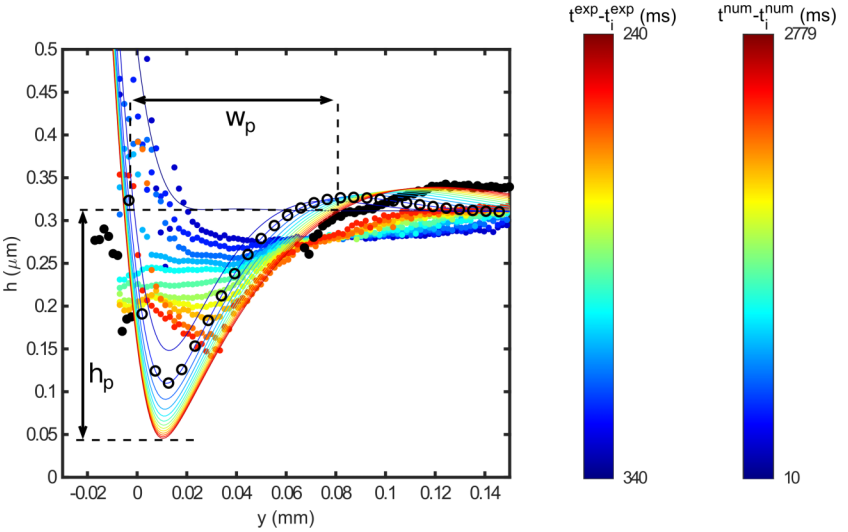

FIG. 9. Film profile evolution with time (in its x-invariant regime). The colored symbols are the experimental profiles [same data as in Fig. 3(b)]. The lines are the numerical profiles obtained by solving Eq. (28); the black empty circles underline the numerical profile corresponding to the same film age as the experimental profile shown in black. The two color bars indicate the time with respect to the initial time t_i for the numerical and experimental results. The last numerical profile, in red, is $h^{\mathrm{num}}(y)$.

on an approximation whose experimental validity is checked in Sec. IV B. Finally, the unstable wavelengths and associated growth rates are discussed in Secs. IV C and IV D.

A. The 1D film profile

We first discuss the x-invariant dynamics occurring between the time $t_i < 0$ and the time $t = 0$ of destabilization.

In the x-invariant case, Eq. (6) becomes

$$\frac{\partial h}{\partial t} = -\frac{\partial}{\partial y}\left[\frac{\gamma_0}{3\eta}h^3\frac{\partial^3 h}{\partial y^3} + v_y h\right]. \tag{28}$$

This equation is solved numerically using a MATLAB code, with the following assumptions. At small y we impose the measured film curvature $1/r_m$. We first impose a positive velocity v_y (oriented toward the film) to prepare a uniform film: using Frankel's theory [1], we choose v_y so that the film converges toward a steady film of half-thickness h_∞, with h_∞ the value measured experimentally at the instability onset. To compare our experimental profile with the Aradian's prediction, the interface velocity is set to 0 at the time defined as the time t_i^{num}, and we let the shape evolve as a function of the numerical time t^{num}. The successive shapes we obtain are plotted in Fig. 9, with a color code indicating the film age. We explored a larger time range in the simulation than in the experiment, so the two color codes differ.

The dynamics of pinching is qualitatively reproduced, but without quantitative agreement, especially at short time. At long time, the sides of the profile are reproduced by the simulation: a very fast thickness increase at the meniscus side, and a milder slope on the film side. However, the position of the minimum is not captured, and the dynamics is faster in the experiment than in the simulation. We explain this by the fact that, at short time, we are not able to stop the interface instantaneously, and some film must be extracted at a slower velocity just before Frankel's film boundary switch direction at t_i (see Sec. II C). Consequently, during a few tens of milliseconds before t_i, instead of pinching a film at rest (Aradian's case [2]), we are extracting a film thinner than

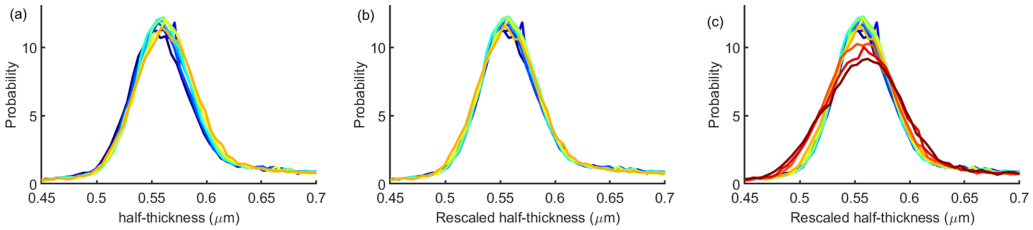

FIG. 10. (a) Probability distribution function of the film half-thickness h in the vicinity of the pinched region, recorded every 5 ms from $t = -10$ ms (dark blue) to $t = 25$ ms (orange). (b) Same data, after a global rescaling, taking into account a residual compression of the film. (c) Same data as in b, with three additional times 30, 35, and 40 ms.

$2h_\infty$ from the meniscus (Frankel's case [1]). The time shift between the experimental and numerical dynamics is thus likely due to the different conditions imposed at short time. Note also that the numerical pinched region width evolves as $t^{1/4}$, and because of this small power law, a small width variation is related to a large time variation.

The profile is expected to relax toward the Aradian's solution at long time, and indeed the numerical and experimental shapes become closer with time. We thus use the numerical shape to rebuild the missing part of the experimental profile at the instability onset. In this regard, we let the numerical film evolve until the best agreement is reached with the measurable part of $h^{\text{exp}}(y, t = 0)$. In Fig. 9, the resulting profile $h^{\text{num}}(y)$ is the last numerical profile, which fits best the two sides of the unstable profile. It is used to determine the geometrical properties of the experimental profile. The numerical profile has a small bump between the thinnest part of the film and the flat film, and thus it reaches the thickness h_∞ at a point located between the pinched region and the bump, which provides a good definition of the end of the pinched region: we define w_p as the width of the domain for which $h^{\text{num}}(y) < h_\infty$. Similarly, the profile depth h_p is defined as $h_\infty - h^{\text{num}}_{\text{min}}$, with $h^{\text{num}}_{\text{min}}$ the minimum value of $h^{\text{num}}(y)$ (see Fig. 9). These two quantities characterize the experimental unstable profile. Note that the fit of the experimental profile relies on the shape and positions of lateral sides of the pinched region. The width w_p is thus a robust experimental quantity, whereas h_p relies on the modeling of the pinch. However, we have shown in Sec. III F that the instability wavelength only depends on w_p, which makes a better determination of h_p much less crucial.

B. Area distribution

One key assumption of the model is that the destabilization occurs at constant thickness distribution. To test this assumption, we measured the probability distribution function $P(h)$ of the film half-thickness in the vicinity of the pinched region. For a film of projected area S_0, this function is defined as $P(h) = (1/S_0)d\hat{S}/(dh)$, with $\hat{S}$ the area defined by Eq. (14). So $P(h)\,dh$ is the fraction of the image having a half-thickness in the range $[h,\ h + dh]$. We selected of small ROI restricted to the pinched region in the images of the film, and we determined the gray level distribution. This distribution is then normalized and converted to obtain $P(h)$. The distributions obtained before and after the instability onset are shown in Fig. 10(a). The most probable thickness is the asymptotic one, $2h_\infty$, and the pinched region contributes to the smaller thicknesses. In Fig. 10(a), we see that the distribution slowly drifts toward larger thicknesses. This indicates a residual compression of the film, which has been corrected in Fig. 10(b) by plotting the distribution of the rescaled half-thickness $h^{\text{res}} = h/[1 + \varepsilon(t)]$. We obtain a very good superposition of all the curves in the range $[-10\,;\,25]$ ms if we assume that ε varies linearly from 0 at $t = -10$ ms (used as an arbitrary reference) to 0.015 at $t = 25$ ms. This indicates that the global film compression during the dynamics is less than 2% and is thus negligible, as is assumed in our model.

More importantly, the rescaled distributions at small thickness are not modified at the instability onset: in Fig. 10(b), the probability distributions are the same before the onset (negative times) and

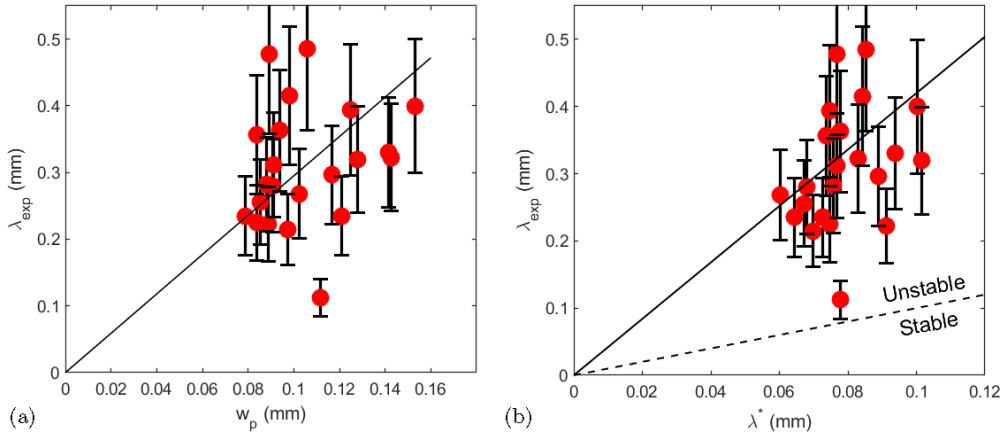

FIG. 11. Experimental wavelength λ_{exp} as a function of the pinched region width (a) and as a function of λ^* (b). The solid lines are guides for the eyes, of the equation $\lambda_{exp} = 2.95 w_p$ on the left and $\lambda_{exp} = 4.2\lambda^*$ on the right. The dashed line corresponds to $\lambda_{exp} = \lambda^*$.

after (positive times). This validates our assumption that the film profile destabilization is governed by a sliding-puzzle dynamics: it confirms that the Poiseuille flow is negligible and that the interface velocity vanishes at the boundary with the meniscus, as discussed in Sec. II C.

This initial destabilization clearly differs from the coarsening process at later times, which has been shown in [17] to be governed by exchanges of film elements between the film and the meniscus: the first one preserves the thickness distribution function, not the second one. To illustrate this point, we added the thickness distribution functions measured in the time range [30, 40] ms after the onset, in Fig. 10(c). In this regime, the film of thickness $2h_\infty$, associated with the maximal area value in Fig. 10, is absorbed by the meniscus, and its probability decreases, while some thin film (of thickness around one micron) is extracted from the meniscus, thus increasing the corresponding probability.

From these graphs, we thus conclude that the film profile destabilization occurs at a constant thickness distribution in the time range [0 ; 25] ms, and that the marginal regeneration, involving interface exchanges with the meniscus, begins afterwards.

C. Unstable wavelength

The Gaussian example illustrates that the patterns with a wavelength larger than a few times the width of the pinched region are more stable than the initial profile, whereas the patterns with a shorter wavelength are less stable. This property is of a purely geometric nature, and it remains true regardless of the physical properties of the system, the initial film thickness, and the minimal thickness in the pinched region. Assuming that the observed wavelength is close to the shorter accessible wavelength, as is obtained for other classical instabilities damped by viscosity, such as the Rayleigh-Taylor instability for example, we thus expect the experimental wavelength to verify $\lambda_{exp} = \alpha w_p$, with α a numerical prefactor close to 1.

This prediction is tested in Fig. 11(a), showing that both quantities are of the same order of magnitude. However, the data dispersion and the narrow range of w_p do not permit us to test the predicted linear dependency.

The pinched region is not Gaussian, so we determined the critical wavelength λ^* of the actual film profile from the numerical profile obtained in Sec. IV A. To perform the film reorganization, we consider a piece of a pinched region of size $w_p \times \lambda$ [the domain $\mathcal{P}_\lambda$, between the two dashed lines in Fig. 12(a)].

The film profile in this domain is discretized and a list of pixels is obtained, sorted by their thickness value. These pixels are then reorganized in concentric circles, from the small thicknesses

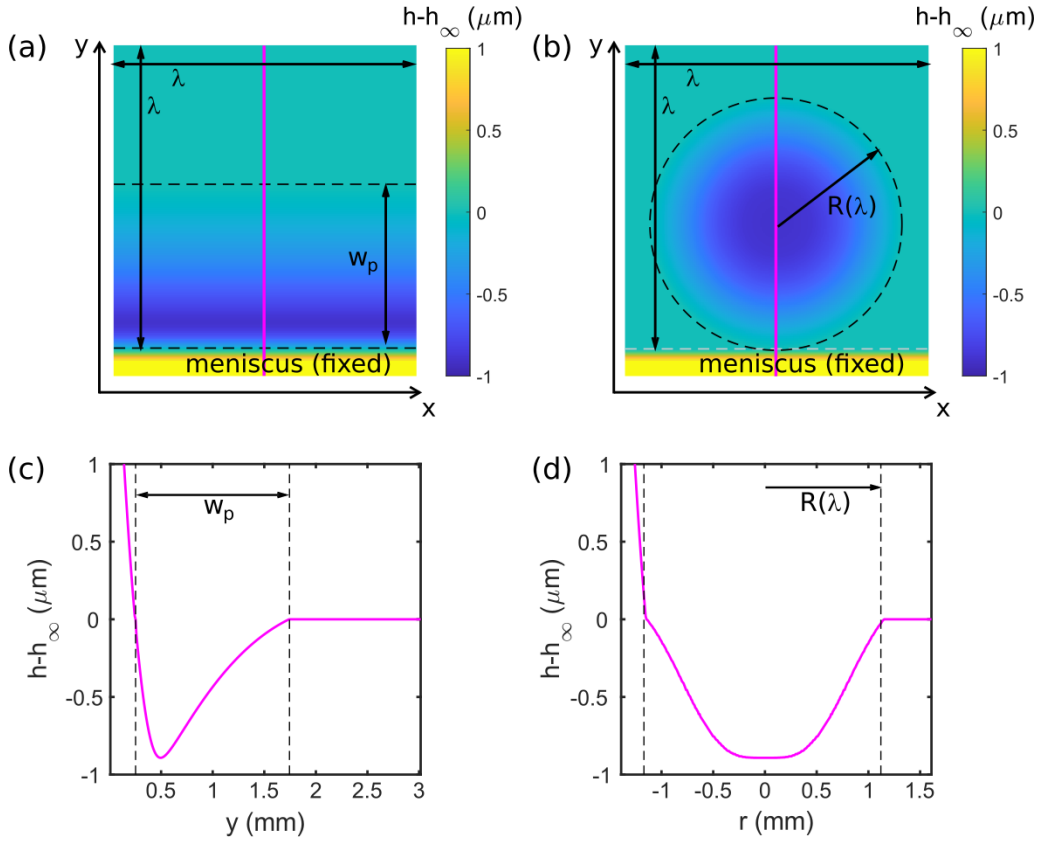

FIG. 12. Example of film profiles before (a) and after (b) the reorganization shown in the (x, y) plane with the color indicating the half-thickness of the film. The reorganized domain $\mathcal{P}_\lambda$ is limited by the black dashed lines. The film domain outside $\mathcal{P}_\lambda$ is the asymptotic flat film of half-thickness h_∞. The thickness profiles along the magenta lines are shown in (c) and (d). The meniscus is shown for clarity [the yellow part in (a) and (b) and the left side of the profile in (c) and (d)] but is not involved in the dynamics.

at the center to the large ones at the perimeter. The rectangle w_p thus becomes a disk of the same area and of radius $R(\lambda) = \sqrt{w_p\lambda}/\pi$ [see Fig. 12(b)]. The periodic pattern of the film profile is the whole pattern shown in Fig. 12(b). The film profile $h^s(r)$ is shown in Fig. 12(d).

The excess area of the obtained axisymmetric spot is $\Delta A_{\text{axi},\lambda} = 2\pi \int_0^{R(\lambda)} (\partial h^s/\partial r)^2/2r\,dr$. For all our profiles, the condition $\Delta A_{\text{axi},\lambda} = \Delta A_{\text{lin}}$ is obtained for $\lambda^* = (0.7 \pm 0.1)w_p$. Note that we verified that $2R(\lambda) < \lambda$ for $\lambda > \lambda^*$, thus allowing us to build the periodic shape without any overlap of the axisymmetric spots for the unstable wavelengths.

The previous analysis evidences that the initial wavelength of the instability must be larger than λ^*. As shown in Fig. 11(b), the observed wavelength verifies $\lambda^{\text{exp}} = (4.2 \pm 1)\lambda^* = (2.8 \pm 0.5)w_p$, so the fastest wavelength appears to be a few times larger than the first unstable one, as expected.

D. Instability growth rate

Entirely solving the problem would require us to determine the time at which the 1D film profile destabilizes, and the corresponding value of w_p. This destabilization time is expected to be governed by very different laws if the initial 1D film profile is unstable or only metastable, which remains an open question. The destabilization time of a metastable profile should be controlled by an external

noise and by the energy barrier between the metastable initial profile and the more stable final one. In contrast, the destabilization time of an unstable profile (or a metastable profile with a small enough energy barrier) is expected to be related to the instability growth rate τ^g.

The scaling law for the growth rate can be deduced from Eq. (15). The instability wavelength λ scales as w_p, so it is the only characteristic length in the film plane. For a piece of film of projected area S, the first term scales as $(\gamma_0/\tau_g)S(h_p/w_p)^2$ and the second one as $\eta S(1/\tau_g)^2$, which leads to the prediction

$$\tau^g = \eta_s w_p^2 / \left(\gamma_0 h_p^2\right). \tag{29}$$

A condition for the instability to be observable is that the pinched region is at least as old as τ^g, which could provide the scaling for the destabilization time $|t_i|$ if the transition dynamics is limited by the instability growth rate. Experimentally, $|t_i|$ is in the range 200–600 ms and $\tau_g \approx 40$ ms.

V. CONCLUSION

In this article, we evidence experimentally that the 1D film thinning process that arises at the boundary between a meniscus and a one-micron-thick horizontal foam film is unstable. These experimental conditions exclude the gravity and the disjoining pressure as potential driving forces for the instability and indicate its purely capillary origin. We identify a class of foam-film flows governed by the thickness gradients only, and preserving the thickness distribution. We show that in this regime, the stable shape is an axisymmetric rearrangements of the initial shape, and that rows of circular pinched regions are metastable shapes, which energy decreases with the wavelength. The predicted instability wavelength deduced from this theory are compatible with the experimental observations. This article identifies the important role of the film thickness gradients in the foam-film dynamics, at the origin of a purely geometric instability, triggering the marginal regeneration.

ACKNOWLEDGMENTS

We thank Luc Hillairet and Serge Cantat for enlightening discussions and for reference to the mathematical theory of rearrangement. This project has received funding from the European Research Council (ERC) under the European Union's Horizon 2020 research and innovation program (Grant Agreement No. 725094).

[1] K. J. Mysels, K. Shinoda, and S. Frankel, *Soap Films: Study of their Thinning and a Bibliography* (Pergamon, New York, 1959).

[2] A. Aradian, E. Raphaël, and P.-G. de Gennes, "Marginal pinching" in soap films, Europhys. Lett. **55**, 834 (2001).

[3] P. D. Howell and H. A. Stone, On the absence of marginal pinching in thin free films, Eur. J. Appl. Math. **16**, 569 (2005).

[4] R. R. Dagastine, R. Manica, S. L. Carnie, D. Y. C. Chan, G. W. Stevens, and F. Grieser, Dynamic forces between two deformable oil droplets in water, Science **313**, 210 (2006).

[5] N. Bremond, A. R. Thiam, and J. Bibette, Decompressing Emulsion Droplets Favors Coalescence, Phys. Rev. Lett. **100**, 024501 (2008).

[6] E. Chatzigiannakis, P. Veenstra, D. ten Bosch, and J. Vermant, Mimicking coalescence using a pressure-controlled dynamic thin film balance, Soft Matter **16**, 9410 (2020).

[7] J. L. Joye, G. J. Hirasaki, and C. A. Miller, Dimple formation and behavior during axisymmetrical foam film drainage, Langmuir **8**, 3083 (1992).

[8] B. Dai and L. G. Leal, The mechanism of surfactant effects on drop coalescence, Phys. Fluids **20**, 040802 (2008).

[9] I. U. Vakarelski, R. Manica, X. Tang, S. J. O'Shea, G. W. Stevens, F. Grieser, R. R. Dagastine, and D. Y. C. Chan, Dynamic interactions between microbubbles in water, Proc. Natl. Acad. Sci. (USA) **107**, 11177 (2010).
[10] H. Lhuissier and E. Villermaux, Bursting bubble aerosols, J. Fluid Mech. **696**, 5 (2012).
[11] L. Champougny, B. Scheid, F. Restagno, J. Vermant, and E. Rio, Surfactant-induced rigidity of interfaces: a unified approach to free and dip-coated films, Soft Matter **11**, 2758 (2015).
[12] D. Y. C. Chan, E. Klaseboer, and R. Manica, Film drainage and coalescence between deformable drops and bubbles, Soft Matter **7**, 2235 (2011).
[13] J.-L. Joye, G. J. Hirasaki, and C. A. Miller, Asymmetric drainage in foam films, Langmuir **10**, 3174 (1994).
[14] J. M. Frostad, D. Tammaro, L. Santollani, S. Bochner de Araujo, and G. G. Fuller, Dynamic fluid-film interferometry as a predictor of bulk foam properties, Soft Matter **12**, 9266 (2016).
[15] S. Andrieux, P. Muller, M. Kaushal, N. S. M. Vera, R. Bollache, C. Honorez, A. Cagna, and W. Drenckhan, Microfluidic thin film pressure balance for the study of complex thin films, Lab Chip **21**, 412 (2021).
[16] R. Bruinsma, Theory of hydrodynamic convection in soap films, Physica A **216**, 59 (1995).
[17] A. Gros, A. Bussonnière, S. Nath, and I. Cantat, Marginal regeneration in a horizontal film: Instability growth law in the nonlinear regime, Phys. Rev. Fluids **6**, 024004 (2021).
[18] H. N. Stein, On marginal regeneration, Adv. Colloid Interface Sci. **34**, 175 (1991).
[19] V. A. Nierstrasz and G. Frens, Marginal regeneration in thin vertical liquid films, J. Colloid Interface Sci. **207**, 209 (1998).
[20] J. Miguet, Amincissement et stabilité de bulles de surface, Ph.D. thesis, Université Paris-Saclay (2019).
[21] Y. Zhang and V. Sharma, Thickness-dependent phase transition drives nanoridge-to-mesa instability in micellar freestanding films, Langmuir **34**, 7922 (2018).
[22] V. Chandran Suja, A. Hadidi, A. Kannan, and G. G. Fuller, Axisymmetry breaking, chaos, and symmetry recovery in bubble film thickness profiles due to evaporation-induced marangoni flows, Phys. Fluids **33**, 012112 (2021).
[23] P. Stevenson, Remarks on the shear viscosity of surfaces stabilised with soluble surfactants, J. Colloid Interface Sci. **290**, 603 (2005).
[24] W. Drenckhan, H. Ritacco, A. Saint-Jalmes, A. Saugey, P. McGuinness, A. Van der Net, D. Langevin, and D. Weaire, Fluid dynamics of rivulet flow between plates, Phys. Fluids **19**, 102101 (2007).
[25] L. Champougny, J. Miguet, R. Henaff, F. Restagno, F. Boulogne, and E. Rio, Influence of evaporation on soap film rupture, Langmuir **34**, 3221 (2018).
[26] J. Seiwert, B. Dollet, and I. Cantat, Theoretical study of the generation of soap films: role of interfacial visco-elasticity, J. Fluid Mech. **739**, 124 (2014).
[27] A. Oron, S. H. Davis, and S. G. Bankoff, Long-scale evolution of thin liquid films, Rev. Mod. Phys. **69**, 931 (1997).
[28] T. Bohr and B. Scheichl, Surface tension and energy conservation in a moving fluid, Phys. Rev. Fluids **6**, L052001 (2021).
[29] G. Pólya and G. Szegö, *Isoperimetric Inequalities in Mathematical Physics (AM-27), Volume 27* (Princeton University Press, Princeton, NJ, 1951).